Enhanced degradation of quinoline in three-dimensional electro-Fenton system using catalytic Fe-Co-Ni-P/g-C₃N₄ particles

Jun Chen[1,,£], Boding Zhang[1,£], Bingxing Wang[1], Chengxing Cui[1], Songlin Wang[1], Jichao Wang[1], Wenlong Zhang2*

[1] College of Chemistry and Chemical Engineering, Henan Institute of Science and Technology, Xinxiang 453003, China,
[2] College of Chemistry, Zhengzhou University, Zhengzhou 450001, China;
[£]Jun Chen and Boding Zhang are co-first authors; They contributed equally to this work.
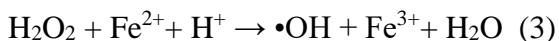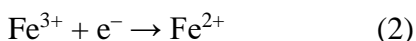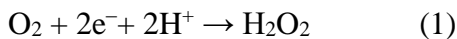[*]E-mail: junchen713@126.com

With high toxicity, carcinogenicity and teratogenicity, quinoline has been threatening human health and ecological environment. Herein, Fe-Co-Ni-P/g-C₃N₄ particles are developed as electrochemical reactors to form a three-dimensional catalytic particle electrode system (3D-CPE) for efficient removal of quinoline from wastewater by electro-Fenton (EF) oxidation process. with reaction time of 30 min, the particles dosage of 50 g/L, pH of 3, conductivity of 11.5 ms/cm, and current density of 37.04 mA/cm², the chemical oxygen demand (COD) removal rate can up to 90.95%. In addition, electron paramagnetic response (EPR) and radical scavenging tests are performed to determine the hydroxyl radicals of electrochemical processes produced. The degradation products are analyzed by high performance liquid chromatography-mass spectrometry (HPLC-MS). Finally, through theoretical calculation and analysis of degradation products, a reasonable degradation mechanism is proposed.

1. INTRODUCTION

Quinoline, as an important raw material, is widely used in rubber, paint, herbicide, metal processing and dyeing industries. However, due to its toxicity, carcinogenicity, mutagenicity and environmental pollution, the degradation of quinoline and its derivatives has received more and more attention in recent years. [1]. Removal of quinoline in wastewater is difficult because of the presence of steric barrier in the bicyclic fused structure and the lengthy photooxidation half-life (10~99 h) [2]. Therefore, an economical and effective quinoline wastewater treatment technology is required.

So far, advanced oxidation processes (AOPs), including ozonation [3], electro-Fenton (EF) oxidation [4], wet catalytic oxidation [5] and photocatalytic oxidation [6], have been employed to remove contaminants from wastewater by producing reinforcing oxidants, such as hydroxyl radical ($\cdot$OH)[7, 8]. EF process, one of the most popular AOPs, has received a lot of attention in the past few years, in which the production of $\cdot$OH does not involve the use of hazardous chemicals [9, 10]. EF process is considered as an electrochemically aided Fenton process. Fenton reagent is produced on the electrode plates (Eqs. 1 and 2) and then reacts to produce $\cdot$OH (Eq. 1), attempting to avoid the consumption of too much H_2O_2 and iron(II) salt. $\cdot$OH can degrade most of organic pollutants in wastewater due to high standard potential (2.80 V/SHE).

$$O_2 + 2e^- + 2H^+ \rightarrow H_2O_2 \qquad (1)$$
$$Fe^{3+} + e^- \rightarrow Fe^{2+} \qquad (2)$$
$$H_2O_2 + Fe^{2+} + H^+ \rightarrow \cdot OH + Fe^{3+} + H_2O \quad (3)$$

However, the traditional EF systems have many unresolved problems, such as low efficiency, small surface area and accumulation of iron mud [11, 12]. Three dimensional EF (3D-EF) systems are developed with high activity and durability, where particle electrodes served as both catalysts and electrodes [13, 14]. The addition of catalytic particle electrodes (CPE) as a third pole provides high current efficiency, large effective electrode area and fast mass transfer rate, thereby improving degradation efficiency of organic pollutants in wastewater [15]. Zhang et al. took Ti, Ti/RuO$_2$ and cobalt loaded powder active carbon as cathode, anode and catalyst, respectively, to construct 3D-CEF system to degrade humic acid [12]. However, high electrode cost hinders the large-scale industrial application. Li et al. used a stainless plate as cathode, a lead alloy as anode and ceramic particles as particle electrodes to decompose pesticide intermediate [16]. It was discovered that the mineralization effect is comparatively ineffective and the COD removal is low (35.17 %).

Due to low cost, stable physical and excellent chemical properties, transition metal phosphides (TMPs) gradually substitute for precious metals. [17]. The combination of the three dimensional electrode and EF systems with TMPs as the particle electrodes has been the subject of only few studies. The particle electrodes can be polarized to shape numerous small electrolytic cells under external electric field conditions. When TMPs are used as particle electrodes, hydroxyl radical can be produced at the anodes of TMPs, and H_2O_2 can be generated at the cathodes, where H_2O_2 breaks down into $\cdot$OH [18]. Carbon nitride with graphitic structure (g-C$_3$N$_4$) has significant potential as non-toxic and pollution-free visible light-driven catalyst because of the special electronic structure [19], providing a good carrier for TMPs.

In this paper, the Fe-Co-Ni-P/g-C3N4 particles were prepared with g-C3N4 as the carrier and loaded with Fe, Co, Ni, P through the solid phase calcination method. For evaluating the effectiveness of quinoline elimination, a 3D-CPE system was built. The Fe-Co-Ni-P/g-C$_3$N$_4$ particles were characterized by X-ray diffraction (XRD), Scanning electron microscopy (SEM), X-ray photoelectron spectroscopy (XPS), transmission electron microscopy (TEM), and pyridine adsorption infrared spectroscopy (Py-IR). The influence of different conditions on the degradation rate of quinoline is systematically studied, including reaction time, dosage of the particle electrodes, pH value, conductivity, and current density. The degradation products were investigated by high-performance liquid

chromatography-mass spectrometry (HPLC-MS), and the degradation mechanism of quinoline was deduced by combining with theoretical calculations.

2. EXPERIMENTAL

2.1 Materials

Melamine, quinoline, $NiSO_4 \cdot 7H_2O$, $Co(NO_3)_2 \cdot 6H_2O$, $FeSO_4 \cdot 7H_2O$, $NaH_2PO_2 \cdot H_2O$, NH_4HCO_3 and $Al(H_2PO_4)_3$ were obtained from Shanghai Macklin Biochemical Co., Ltd. H_2SO_4 and H_2O_2 were purchased from Yantai Shuangshuang Chemical Co., Ltd. polyacrylamide (PAM), Tert butanol (t-BuOH), NaOH, and NaCl were purchased from Shanghai Aladdin Biochemical Technology Co., Ltd. None of the chemicals were further purified before usage.

2.2 Synthesis of g-C$_3$N$_4$

100 g of melamine was packed into a 200 ml crucible and calcined in a muffle furnace at a temperature increase of 10 °C/min for 2 h at 550 °C. After cooling to room temperature, a lump of yellow g-C$_3$N$_4$ was obtained and then ground into a powder.

2.3 Preparation of Fe-Co-Ni-P/g-C$_3$N$_4$ particles

The prepared g-C$_3$N$_4$ (45.5 g) was dispersed in appropriate amount of deionized water with ultrasonic stirring for 45 min. Meanwhile, certain amounts of $FeSO_4 \cdot 7H_2O$ (22.8 g), $Co(NO_3)_2 \cdot 6H_2O$ (11.9 g) and $NiSO_4 \cdot 7H_2O$ (10.8 g) were dissolved to generate a clear solution, and then the solution was added by drop into the g-C$_3$N$_4$ suspension. The above mixture was stirred uniformly for 1 h by means of a magnetic stirrer and then dried at 100 °C by vacuum oven. After cooling, the finished product was carefully crushed into powder in a mortar rinsed with deionised water and dried at 70 °C in a vacuum oven to obtain Fe-Co-Ni/g-C$_3$N$_4$. Fe-Co-Ni-P/g-C$_3$N$_4$ particles were prepared by thermally phosphorylating Fe-Co-Ni/g-C$_3$N$_4$. Briefly, 10.7 g of Fe-Co-Ni/g-C$_3$N$_4$ and 7.1 g of $NaH_2PO_2 \cdot H_2O$ were mechanically mixed and ground to a homogeneous powder in a mortar. The mixture was then calcined at 300 °C in a nitrogen atmosphere for 2 h. Samples labelled as Fe-Co-Ni-P/g-C$_3$N$_4$ composites were washed 5 times with deionised water and then dried in an oven. Fe-Co-Ni-P/g-C$_3$N$_4$ composites, $Al(H_2PO_4)_3$ and NH_4HCO_3 with a mass percentage of 95%, 4%, 1% were mixed and granulated evenly, where $Al(H_2PO_4)_3$ and NH_4HCO_3 were used as binders and pore-forming agents, respectively. The pretreated particles were heated up to 300 °C at 5 °C/min in a vacuum tube furnace and calcined for 2 h under nitrogen atmosphere. Finally, Fe-Co-Ni-P/g-C$_3$N$_4$ particles were obtained. The original Fe-Co-Ni-P was prepared in a similar way, without the addition of g-C$_3$N$_4$.

2.4 Experimental setup

The volume of three-dimensional electrochemical reactor was 2 L, which was made of polypropylene. The two stainless steel plates were used as anode and cathode, respectively, with the distance of 10 cm between them. The effective area of each electrode plate was 9 cm × 15 cm. Particle electrodes were filled between the electrode plates. An aeration pump was used to inject the air and accelerate the mass transfer process. The schematic diagram was showed in Figure S1.

2.5 Characterization techniques

Microscopic images, structural morphology and compositional data of the CPE were obtained using SEM (Quanta 200, FEI, America), TEM (JEM-2100F, JEOL, Japan), XPS (Kratos Axis Ultra DLD, SHIMADZU, Japan) and XRD (D8-Advance, Bruker, Germany). The catalyst's acidity was determined with Py-IR (Nicolet6700, Thermo Fisher Scientific, America). EPR (A300, Bruker, Germany) analyses and quenching tests was performed to identify the hydroxyl radicals in the electrochemical processes. X-ray photoelectron spectroscopy measurements were carried out using unmonochromatized Al Ka line at 1486.6 eV (12 kV with 20 mA anode current) and a Leybold EA-11 analyzer with constant pass energy of 100 eV. X-ray diffraction analysis was performed using a Cu Kα source operated at 40 kV and 40 mA. The diffraction patterns were recorded in the range 10° to 80°. Pyridine adsorption infrared spectroscopy were measured using a Nicolet 6700 smart Fourier transform pyridine infrared spectrometer from Thermo Fisher Scientific, America, with a resolution of 4 cm^{-1}. Electron paramagnetic resonance spectrometer parameters included a center field at 3510 G and a sweep width of 100 G.

2.6 Quinoline degradation procedure

Deionized water was used to prepare simulated quinoline wastewater (1.0 g/L). The particle electrodes were placed in the quinoline solution for 24 h prior to the electrolysis to avoid the effect of CPE adsorption on the electrolysis experiments. The circumstances for all trials were galvanostatic. To measure the COD concentrations, samples are collected after degradation at specific time intervals. The parameters affecting the degradation efficiency of quinoline, such as initial pH value, conductivity, H_2O_2 concentration, voltage, current density and dosage, were examined. HPLC-MS was also used to identify the quinoline's degradation products.

2.7 Analytical methods

The amount of organics in wastewater can be indirectly measured by using the COD [20]. The COD concentrations were measured with an intelligent multi-parameter digester (LH-25A) and a multi-parameter water quality analyzer (5B-3B(V8), Beijing Lianhua YongXing Science and Technology

Development Co.,Ltd, China). The COD removal rate of wastewater could be calculated with Equation (4):

$$\text{COD removal efficiency}(\%) = \frac{(C_i - C_t)}{C_i} \times 100\% \quad (4)$$

where C_i and C_t denote the concentration of COD in the feed solution and the treated solution, respectively.

Degradation products were investigated by high performance liquid chromatography and quadrupole time-of-flight mass spectrometry (HPLC, 1290; Q-TOF-MS, 6530, Agilent, America) with a TC-C18 column (4.6 mm × 250 mm, 5 µm). The mobile phase was 0.1% formic acid water and methanol, with a volume ratio of 20:80 and a flow rate of 0.4 mL/min.

3. RESULTS AND DICUSSION

3.1 CPE characterization

Figure 1 exhibits the SEM images of g-C$_3$N$_4$, Fe-Co-Ni-P, Fe-Co-Ni-P/g-C$_3$N$_4$ composites and Fe-Co-Ni-P/g-C$_3$N$_4$ particles. Massive irregular small crystals are observed on the rough g-C$_3$N$_4$ (Figure 1(a)). It is clear that Fe-Co-Ni-P nanoparticles connect with each other through thin sheets (Figure 1(b)). The prepared Fe-Co-Ni-P/g-C$_3$N$_4$ composites are aggregated into a highly folded structure (Figure 1(c)). As shown in Figure 1(d), the Fe-Co-Ni-P/g-C$_3$N$_4$ particles show a relatively smooth interface and a large number of channels, which may increase active sites. The elemental mapping by energy dispersive x-ray spectroscopy (EDS) shows the presence of Fe, Co, Ni, P, C and N (Fig. S2), suggesting that the Fe-Co-Ni-P was successfully supported on the pristine g-C$_3$N$_4$.

The TEM images were used to identify the morphological characteristics and structures. The as-prepared g-C$_3$N$_4$ shows flaky with microscale layers (Figure 1(e)). Figure 1(f) shows that the size of the Fe-Co-Ni-P nanoparticles is ca 100−200 nm. In Figure 1(g), the gray small particles are the g-C$_3$N$_4$ support, and the black large particles are the Fe-Ni-Co-P. It was found that Fe-Co-Ni-P is closely embedded in the g-C$_3$N$_4$ surface, forming a co-catalyst composite (Figure 1(g)). For Fe-Co-Ni-P/g-C$_3$N$_4$ particles (Figure 1 (h)), Fe-Co-Ni-P is densely and completely wrapped in g-C$_3$N4, possibly due to the action of binder.

The successful preparation of g-C$_3$N$_4$ and Fe-Co-Ni-P/g-C$_3$N$_4$ particles was demonstrated by XRD analysis. As shown in Figure 2, for both samples, two characteristic diffraction peaks are detected in the (100) plane of g-C$_3$N$_4$ with repeating cycles in the heptathiazine framework plane and the (002) plane of interlayer stacking of conjugated aromatic structures, which are located at 12.8° and 27.5°, respectively [21].
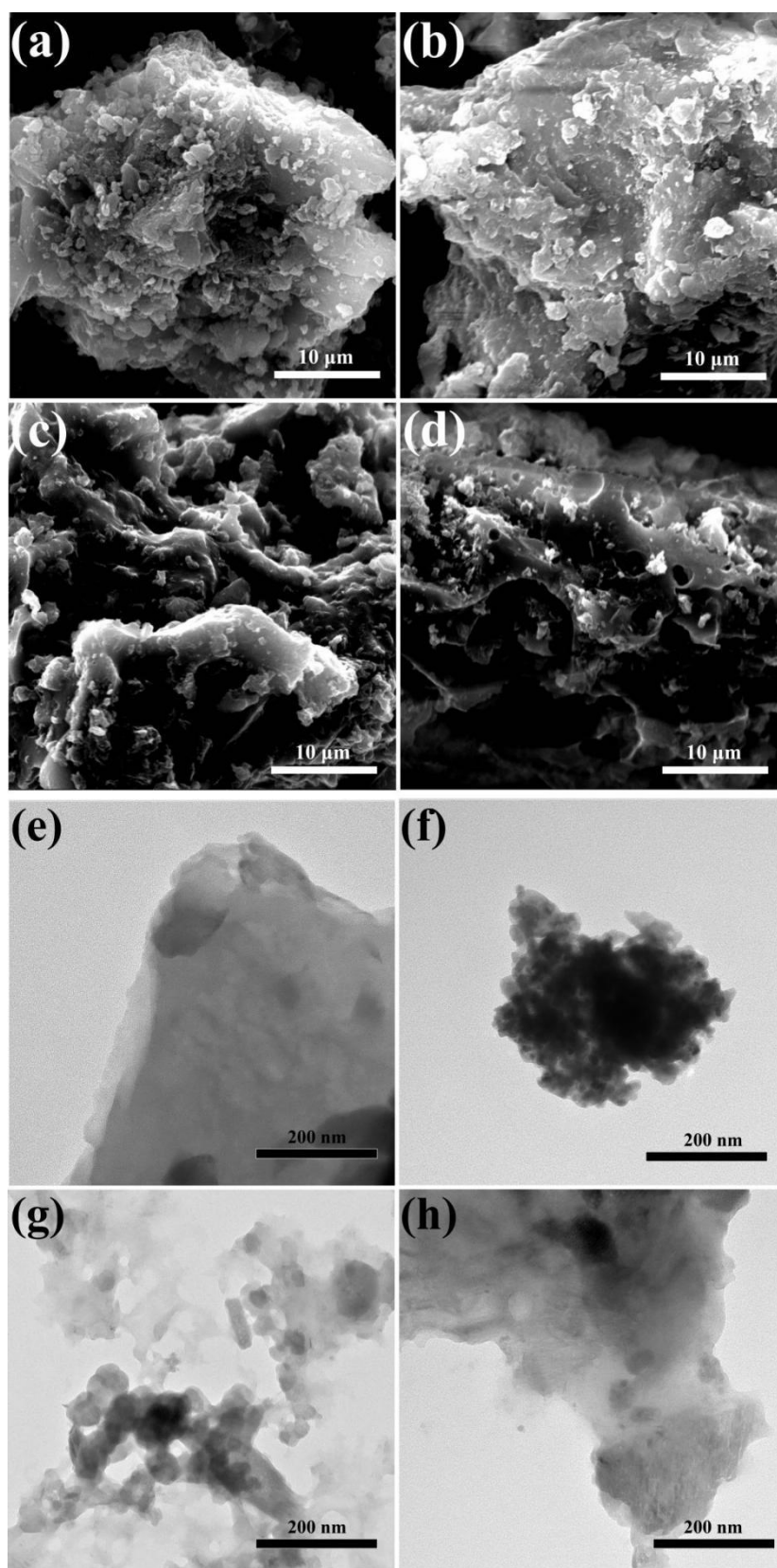
Figure 1. Scanning electron microscopy images of (a) g-C$_3$N$_4$, (b) Fe-Co-Ni-P, (c) Fe-Co-Ni-P/C$_3$N$_4$ composites, (d) Fe-Co-Ni-P/g-C$_3$N$_4$ particles. Transmission electron microscopy images of (e) g-C$_3$N$_4$, (f) Fe-Co-Ni-P, (g) Fe-Co-Ni-P/C$_3$N$_4$ composites , (h) Fe-Co-Ni-P/g-C$_3$N$_4$ particles.

The peaks of 31.7°, 35.7° and 38.2° are attributed to FeP$_4$ (JCPDS No. 71-0482). The characteristic peaks located at 41.1° and 45.0° are attributed to CoNiP (JCPDS No. 71-2336). According to the XRD results, the Fe-Co-Ni-P/g-C$_3$N$_4$ particles is successfully fabricated by loading Fe, Co, and Ni metal phosphides onto g-C$_3$N$_4$.
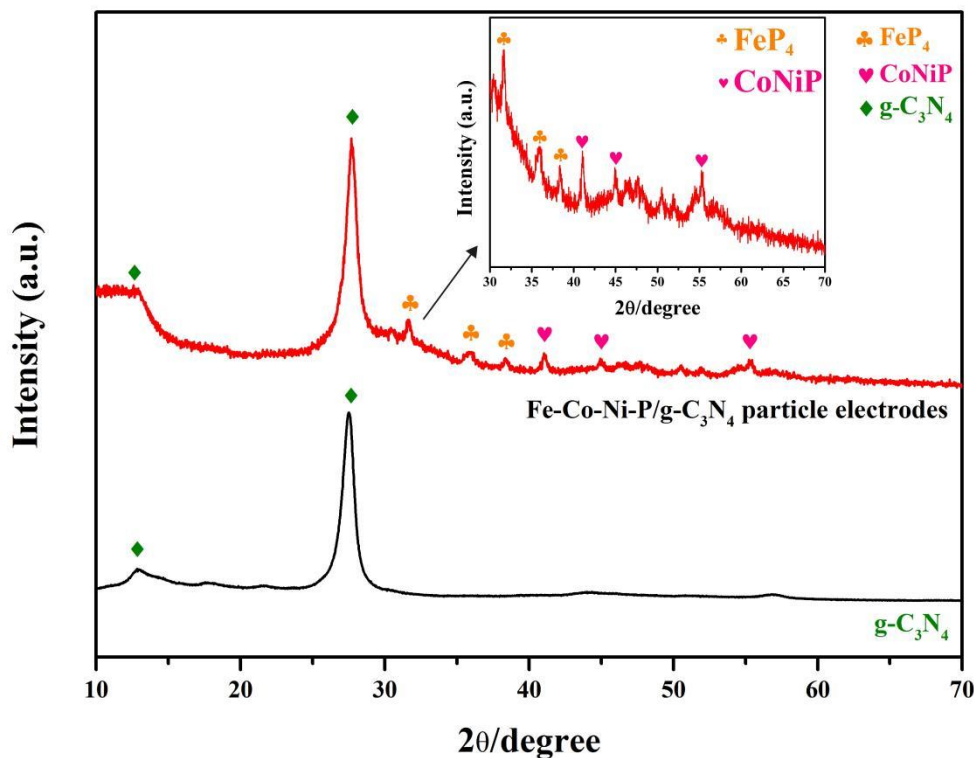
Figure 2. XRD patterns of g-C$_3$N$_4$ and Fe-Co-Ni-P/g-C$_3$N$_4$ particles.

The surface elemental states and electronic structure of the Fe-Co-Ni-P/g-C$_3$N$_4$ particles were further probed using XPS. The Fe, Co, Ni, P, C and N exist in the Fe-Co-Ni-P/g-C$_3$N$_4$ particles according to XPS survey scans. The Fe 2p spectrum (Figure 3(a)) shows two primary peaks at 706.2 and 719.7 eV, coupled by two satellite peaks (labeled as "Sat.") at 714.1 and 731.3 eV relating to Fe^{3+} 2p$_{3/2}$ and Fe^{3+} 2p$_{1/2}$, respectively [22]. The other two distinct peaks at binding energies of 709.1 and 724.9 eV corresponds to Fe^{2+} 2p$_{3/2}$ and Fe^{2+} 2p$_{1/2}$, respectively [23], suggesting the co-existence of Fe^{3+} and Fe^{2+} in the Fe-Co-Ni-P/g-C$_3$N$_4$ particles [24]. In the Co 2p spectrum, there can be significant peaks at 780.2 eV and 795.8 eV due to the formation of CoP as shown in Figure 3(b). The presence of cobalt oxides was also indicated by the peaks at 783.3 eV and 800.5 eV. Furthermore, The peaks at 803.2 and 786.6 eV belong to the satellite peaks of Co 2p$_{1/2}$ and Co 2p$_{3/2}$.[25]. The Ni 2p spectrum clearly shows two spin–orbit doublets of Ni 2p$_{3/2}$ and Ni 2p$_{1/2}$, while satellites can be observed at 859.8 eV and 879.1 eV as in Figure 3(c) [26] [27]. The peaks at 854.6 eV and 869.3 eV could be designated to the metal Ni. Meanwhile, the peaks at 855.1 and 872.7 eV correspond to the oxidized Ni [28]. A peak of 131.8 eV was observed in the P 2p spectrum corresponding to P 2p$_{3/2}$ on the surface of the sample. In addition, as shown in Figure 3(d), there is a peak at 132.6 eV due to the presence of phosphorus oxide [29]. In Figure

3(e), The C 1s spectrum has three peaks at 288.4 eV, 285.2 eV and 284.7 eV corresponding to O=C-O, -C-P and -C=C, respectively [30]. In the N 1s spectrum (Figure 3(f)), three peaks at 398.5 eV, 399.2 eV and 400.8 eV are caused by the sp^2 hybrid aromatic N atom (N-N=C), the tertiary nitrogen in the N-(C)^3 group and the terminal amino functional group (C-N-H), respectively.
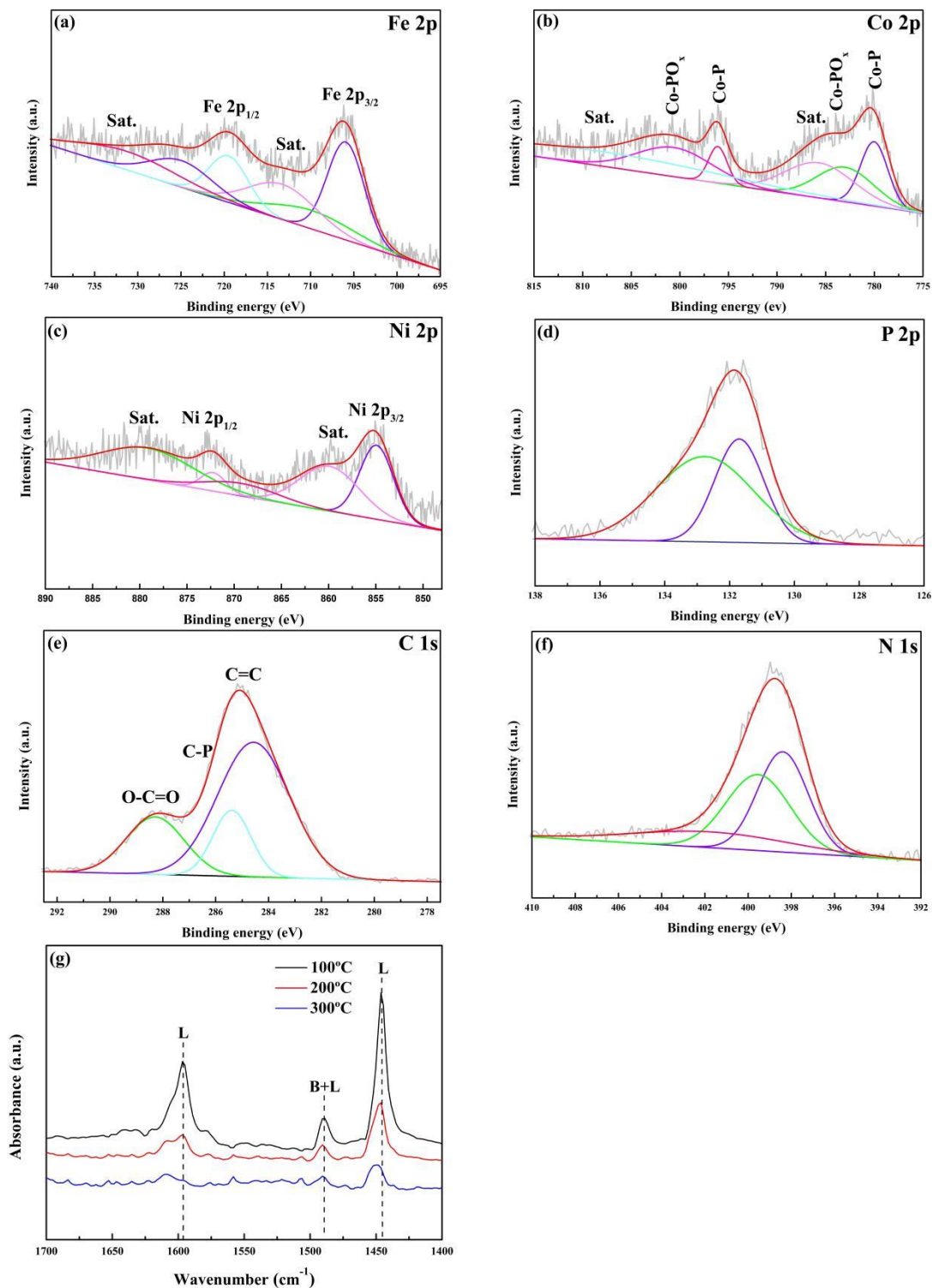
Figure 3. XPS spectra of Fe-Co-Ni-P/g-C$_3$N$_4$ particles: (a) Fe 2p; (b) Co 2p; (c) Ni 2p; (d) p 2p; (e) C 1s; (f) N 1s. (g) Py-IR spectra.

After doping Fe-Co-Ni-P with g-C_3N_4, the binding energy of C 1s and N 1s in Fe-Co-Ni-P/g-C_3N_4 particles moves to higher energies, indicating the existence of internal forces between Fe-Co-Ni-P and g-C_3N_4 [31]. The incorporation of P with nontoxic metallic elements of Co^{2+}/Co^{3+}, Fe^{2+}/Fe^{3+} and Ni^{2+} could significantly boost the amount of available active sites and further improve the catalytic activities for wastewater treatment. The results demonstrate that Fe-Co-Ni-P/g-C_3N_4 particles are successfully fabricated.

In order to demonstrate the existence of Lewis (L) acid site and Brünsted (B) acid site type in the Fe-Co-Ni-P/g-C_3N_4 particles, the CPE was characterized by Py-IR. As shown in Figure 3(g), the absorption peaks at the acidic site of L acid are 1595 cm^{-1} and 1445 cm^{-1}.The absorption peak near 1485 cm^{-1} is a synergy between the B and L acid sites [32] [33]. No obvious absorption peak near 1540 cm^{-1} is observed, indicating that the amount of B acid is less than the L acid [34]. Table S1 shows the results of Py-IR spectral analysis. The content of the B acid site decreases slightly and that of the L acid site decreased sharply from 41.38 μmol/g to 6.66 μmol/g, with increasing temperature. Based on the results, it can be demonstrated that Fe-Co-Ni-P/g-C_3N_4 particles is a solid catalyst dominated by L acid sites, which could facilitate the high catalytic stability in an aqueous medium.

*3.2 Effect of parameters on quinoline removal*

Operation parameters, including reaction time, catalyst dosage, initial pH, electrical conductivity and current density, were investigated for the quinoline degradation in the 3D-CPE system (Figure 4). Single-factor experiment was conducted to optimize the experimental conditions.

As can be seen from Figure 4(a), the removal efficiency of COD increases as the increase of reaction time. The highest COD degradation rate (90.95%) can be achieved after 30 min of treatment. The rapid decrease of COD in the first 30 min is attributed to the oxidative degradation of quinoline by free radicals [35]. After 30 min, the efficiency of the COD removal remained nearly stable, which could be attributed to the formation of undegradable by-products. The pH of the wastewater increases with the increase of reaction time, resulting in the formation of colloidal substances or flocculent precipitates of Fe^{3+} and Fe^{2+} [36]. The colloidal substances or flocculent precipitates will cover the cathode/anode plates and the third electrode surface, weakening the mass transfer efficiency of the particle electrode. Hence, the optimal reaction time of 30 min is chosen in the subsequent tests.

Another crucial factor is the dosage of Fe-Co-Ni-P/g-C_3N_4 particles. The elimination rate of quinoline rises from 59.16% to 90.95% with the increase of the dosage of the CPE from 20 g/L to 50 g/L at 30 min, as shown in Figure 4(b), which may be due to the increase in the number of active sites, resulting in a large number of hydroxyl radicals. However, when the dosage of the CPE is further increased from 50 g/L to 60 g/L, the COD removal rate decreases. This is most likely due to the obstruction of the mass transfer process by the excess CPE, which affects the removal of quinoline [37]. Here, the dosage is optimized to be 50 g/L for the COD removal.

The pH played an important role in the degradation of wastewater [38]. As shown in Figure 4(c), the highest COD degradation rate (87.14%) can be achieved after 30 min when the initial pH is set to 3. However, regardless of the initial pH increases or decreases, the general COD removal rate declines.

The low pH usually facilitates the degradation of pollutants in the EF system [39]. The acidic solution leads to the side reaction of hydrogen evolution on the cathode and suppressed the oxygen evolution reaction [40], which accelerates the degradation of organic pollutants on the anodes or Fe-Co-Ni-P/g-C_3N_4 particles.
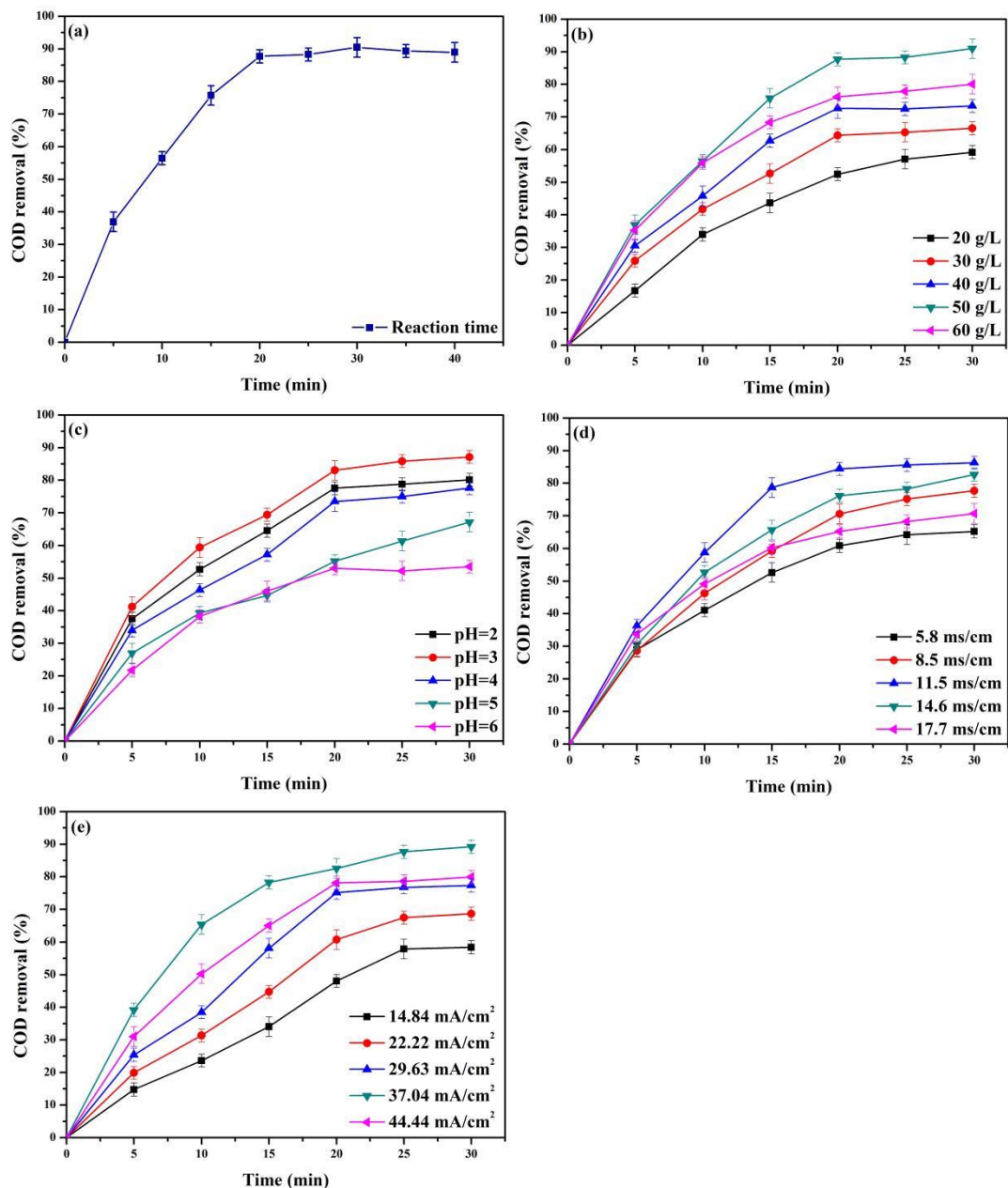
Figure 4. Effects of operational parameters on COD removal rate: (a) reaction time; (b) dosage; (c) pH; (d) electrical conductivity; (e) current density.

Due to the doping of Fe, Co, Ni and P, a large number of free radicals are generated on the surface of Fe-Co-Ni-P/g-C_3N_4 particles, which promotes the degradation of quinoline and the removal of COD. However, high H^+ concentration could reduce the transition metal phosphides in the particle electrodes, thus lowering the catalytic activity. Moreover, with the high initial pH, the side reaction of the oxygen

evolution is intensified, reducing the reaction current efficiency and the degradation efficiency [41]. As a result, the ideal initial pH was set to be 3.

NaCl is utilized as supporting electrolyte to improve the conductivity in this study. Chlorine evolution reaction is not excluded, which could result in secondary chlorine oxidation reaction, facilitating the oxidative degradation of organic materials [42]. The COD degradation rate increases gradually with increasing conductivity. As displayed in Figure 4(d), the maximum COD degradation (86.29 %) is achieved when the conductivity is 11.5 ms/cm. The supporting electrolyte facilitates the electron transfer in the EF reaction, which accelerates the elimination of quinoline [43]. When the conductivity is raised from 11.5 ms/cm to 17.7 ms/cm, the efficiency of COD removal decreases from 86.29 % to 70.68 %. Excess electrolyte could cover the surfaces of the 3D-CPE under the electric field, which hampers the production of catalytic active substances.

Figure 4 (e) displays the impact of the current density on COD elimination in the 3D-CPE. The efficiency of quinoline degradation is significantly enhanced after 30 min of the treatment with the raise of the current density in the range 14.84 - 37.04 mA/cm^2. When the current density is boosted beyond 44.44 mA/cm^2, the COD removal rate decreases. This finding demonstrated that a large current might produce more H_2O_2 and •OH radicals, which is beneficial to the removal of the contaminants [44]. However, excessive current density will lead to undesirable side reactions. For example, the •OH generated in the reaction are consumed by the oxygen evolution reaction [45]. Accordingly, the current density of 37.04 mA/cm^2 is the optimum value in this study.
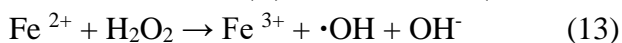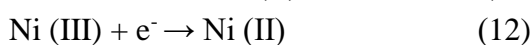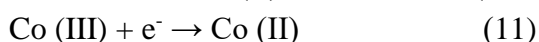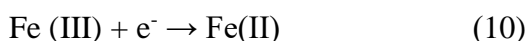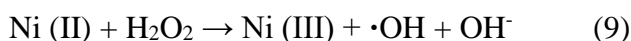
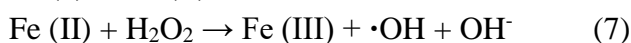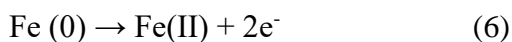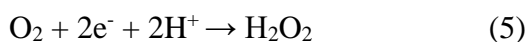*3.3 Investigation on the material stability*

The stability of the Fe-Co-Ni-P/g-C$_3$N$_4$ CPE was tested through consecutive 3D-CPE system under the optimal circumstances. As shown in Figure S3, after 30 days of operation, the COD removal efficiency decreases only about 5.9%, but still maintains more than 85%. The decrease in degradation efficiency may be due to the leaching of ions from the reaction, which reduces the catalytic performance. Overall, CPE has a high removal rate for quinoline wastewater. At the same time, the resistivity of particle electrodes and the energy consumption of 3D-CPE system are studied and shown in the supplementary materials. The results show that the particle electrodes have higher resistance (1.2×10^5 $\Omega\cdot$cm) and the 3D-CPE system has lower energy consumption (11.45 kWh/kg quinoline).
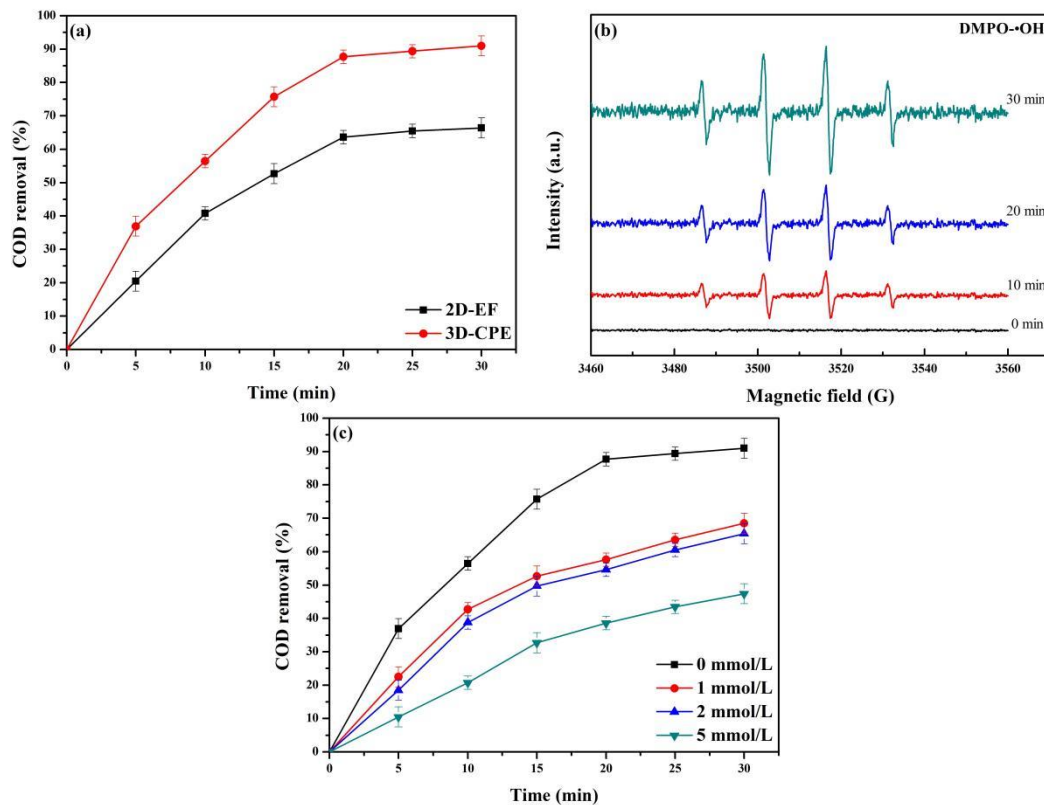
3.4 Catalytic mechanism

The comparison between the two-dimensional and three-dimensional EF systems (Figure 5(a)) shows that the degradation rate increases sharply in the presence of particle electrodes. Previous research have found that the •OH can be consecutively generated in the 3D electrochemical system [46]. The electron paramagnetic response (EPR) was used in this experiment to identify the •OH [47]. It is discovered that the DMPO-•OH adducts has a 4-fold characteristic peak, implying that the •OH is generated (Fig. 5(b)) [48]. Furthermore, the •OH content of the system increases steadily with time. Quenching experiments were performed with the free radical scavenger (t-BuOH) [49]. Figure 5(c)

shows that the COD removal efficiency drastically diminishes with the increase of t-BuOH concentration. The degradation rate of COD is 46.38% after 30 min of treatment when the concentration of t-BuOH is 5.00 mmol/L. With the addition of t-BuOH, the •OH generated by Fenton and Fenton-like reactions is consumed. The decrease of •OH inhibits the degradation of quinoline and the elimination of COD. These results suggest that ·OH plays an influential role in the degradation of quinoline in the 3D-CPE system.

Based on the discussion above, it is suggested that the produced •OH promotes the removal efficiency of quinoline in the 3D-CPE system (Fig. (6)). g-C$_3$N$_4$ with large surface area, offers massive active sites for the catalytic degradation of quinoline. Fe, Co, and Ni loaded on the g-C$_3$N$_4$ surface are the catalytically active species in the Fenton and Fenton-like reaction. The potential mechanism is proposed as follows. Firstly, heterogeneous catalytic processes occur on the surface of the electrode plates and the particle electrodes. At the cathode and Fe-Co-Ni-P/g-C$_3$N$_4$ particles, O$_2$ is reduced to H$_2$O$_2$ (Eq. (5)). Fenton reactions occur on the surface of the anode plates and Fe-Co-Ni-P/g-C$_3$N$_4$ particles. Under the action of the current, Fe(0) is oxidized to Fe(II) during the reaction (Eq. (6)). Then the classical Fenton reactions occur on the surface to generate •OH to oxidize the pollutants, and Fe(II) is oxidized to Fe(III) (Eq. (7)), simultaneously [37]. The Fenton-like reaction also generated •OH on the surface of the particle electrodes through the Co(II)/Co(III) and Ni(II)/Ni(III) redox processes (Eqs. (8) and (9)). Subsequently, Fe(III), Co(III) and Ni(III) are reduced to Fe(II), Co(II) and Ni(II) after gaining electrons in solution, and adsorbed on Fe-Co-Ni-P/g-C$_3$N$_4$ particles (Eqs. (10), (11) and (12)). Secondly, the homogeneous Fenton reaction involves Fe^{2+} (Eqs. (13)) because some of the Fe would leak into the solution [50]. Finally, the •OH radicals attacked the quinoline molecules, which degraded into inferior products (Eq. (14)). Moreover, the presence of P with negative charge in Fe-Co-Ni-P/g-C$_3$N$_4$ particles is favorable for negative shift as electron donor, which accelerates the charge transfer [51]. On the whole, the advanced oxidation technology by using the 3D-CPE system is the coupling of the electro-Fenton method and the three-dimensional electrode method, which can simultaneously carry out direct anodic oxidation, cathodic reduction to produce H$_2$O$_2$, Fe^{2+} catalyzed Fenton reaction, ·OH indirect oxidation, particle electrode adsorption, particle electrode catalytic oxidation. It is an integrated electrochemical oxidation technology with multiple effects as shown in Figure 6.

$$O_2 + 2e^- + 2H^+ \rightarrow H_2O_2 \tag{5}$$

$$Fe\,(0) \rightarrow Fe(II) + 2e^- \tag{6}$$

$$Fe\,(II) + H_2O_2 \rightarrow Fe\,(III) + \cdot OH + OH^- \tag{7}$$

$$Co\,(II) + H_2O_2 \rightarrow Co\,(III) + \cdot OH + OH^- \tag{8}$$

$$Ni\,(II) + H_2O_2 \rightarrow Ni\,(III) + \cdot OH + OH^- \tag{9}$$

$$Fe\,(III) + e^- \rightarrow Fe(II) \tag{10}$$

$$Co\,(III) + e^- \rightarrow Co\,(II) \tag{11}$$

$$Ni\,(III) + e^- \rightarrow Ni\,(II) \tag{12}$$

$$Fe^{2+} + H_2O_2 \rightarrow Fe^{3+} + \cdot OH + OH^- \tag{13}$$

$$\cdot OH + Quinoline \rightarrow Degraded\ products \tag{14}$$

Figure 5. (a) Comparison of the COD removal rate between 2D-EF and 3D-CPE; 2D-EF conditions: Reaction period of 30 min, pH of 3, electrical conductivity of 11.5 ms/cm, and current density of 37.04 mA/cm^2; (b) EPR detection spectra; (c) Effect of t-BuOH dosage on the rate of the COD removal under 3D-CPE.
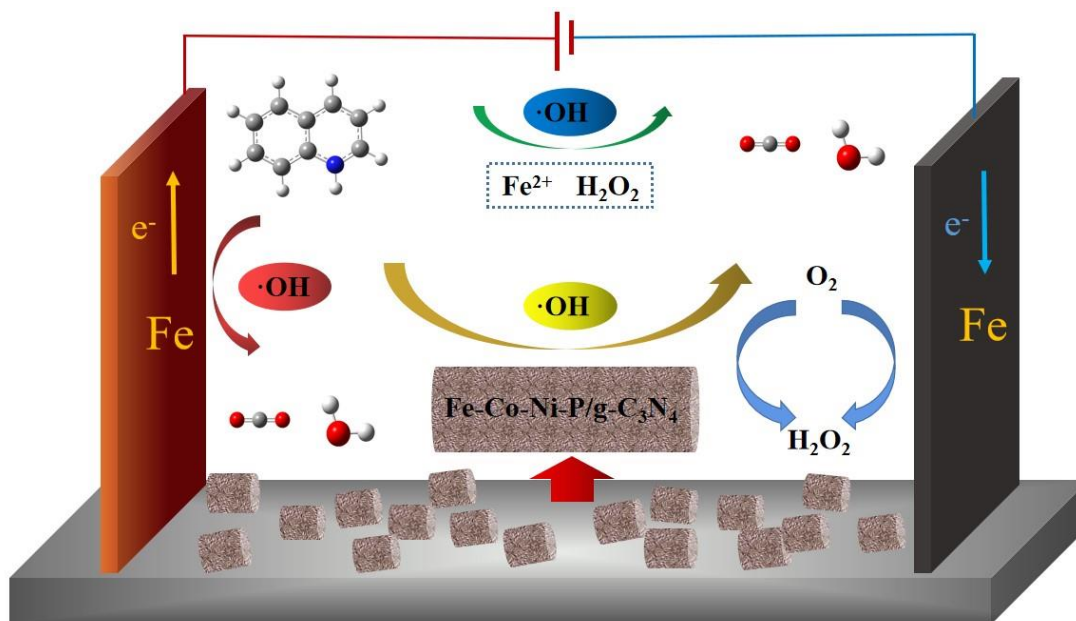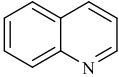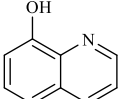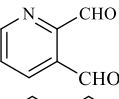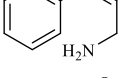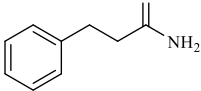

Figure 6. Proposed catalytic mechanism of 3D-CPE system.

3.5 Degradation pathways

The color, pH value, and COD clearly vary with the reaction time in the heterogeneous 3D-CPE process of quinoline, indicating the generation of some intermediate byproducts. HPLC-MS was used to determine the possible molecular structure of the degradation products (Figure S4-S5 and Table 1). Two potential quinoline degradation pathways and the reaction energies for each step were inferred (Figure S6). Density functional theory (DFT) calculations were also performed for these pathways at the MN15L/6-311G (d) level, taking into account the solvent effect [52]. Pathway I is an exergonic process which release Gibbs free energy of -3.42 kcal/mol, while Pathway II is essentially endergonic. Consequently, only the first pathway is discussed in detail here.

Table 1. Possible major intermediates in the quinoline degradation process.

Compound	Molecular weight	Tentative structure
Quinoline	129.1	
8-Hydroxyquinoline	145.1	
2.3-pyridinedicarboxyaldehyde	133.1	
(Z)-3-phenylprop-2-en-1-amine	133.1	
Phenylpropanamide	149.2	

Pathway I was •OH directly attacks the 8th position on the benzene ring and undergoes an addition reaction with it due to the relatively high π-charge density of the C-atom at the 8th position in the benzene ring part of the quinoline molecule, which makes the electrophile substitution reaction usually attack this position. After dehydrogenation of 5,8-dihydroxyquinoline, 5,8-quinolinedione is formed. Under the oxidation of •OH, the benzene ring is opened at position 5 and position 8 to form the unstable intermediate product 2,3-pyridinedicarboxaldehyde, which is further oxidized to 2-pyridinedicarboxaldehyde. Finally, these nitrogen-containing intermediate compounds were mineralized to form small molecules.

Another potential degradation pathway is as follows. Because •OH is a strong electrophilic reagent, organic contaminants were generally degraded via electrophilic addition reactions. As a result, the hydroxyl radical was the first to attack the nitrogen ring of the quinoline, which is similar to Jiao's quinoline degradation path in catalytic wet peroxide oxidation with CuO-doped Ce catalyst [53]. The potential pathway was shown in Figure S6 Pathway 2.

4. CONCLUSION

This contribution describes the successful synthesis of Fe-Co-Ni-P/g-C$_3$N$_4$ particles as non-precious metal catalysts and the construction of a 3D-CPE system to investigate the degradation of quinoline wastewater. The highest quinoline removal rate of 90.95% can be achieved at particle dosage of 50 g/L, pH of 3, electrical conductivity of 11.5 ms/cm, current density of 37.04 mA/cm^2 and electrolysis time of 30 min. The 30 days consecutive tests show excellent mineralization efficiency, indicating that the Fe-Co-Ni-P/g-C$_3$N$_4$ particles are stable and reusable Fenton-like catalysts. Furthermore, the potential mechanism and pathway of quinoline degradation in 3D-CPE system is proposed by EPR detection spectroscopy and HPLC-MS analysis. The degradation of quinoline begins with the cleavage of the benzene or pyridine ring under the attack of hydroxyl radicals. Finally, quinoline is mineralized into small molecules. This study shows the potential application of Fe-Co-Ni-P/g-C3N4 particles based 3D-CPE system in wastewater treatment.

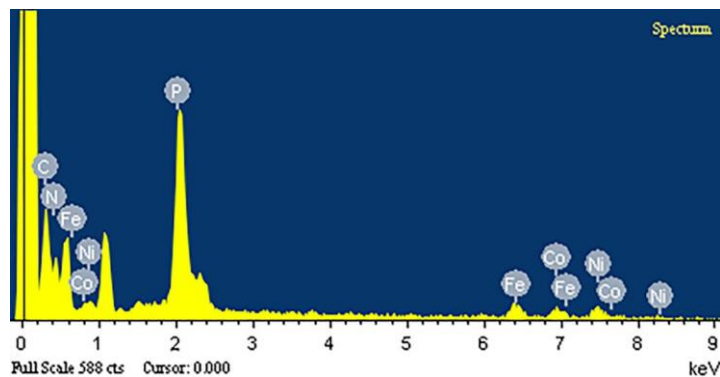SUPPLEMENTARY MATERIALS:

Experimental Setup
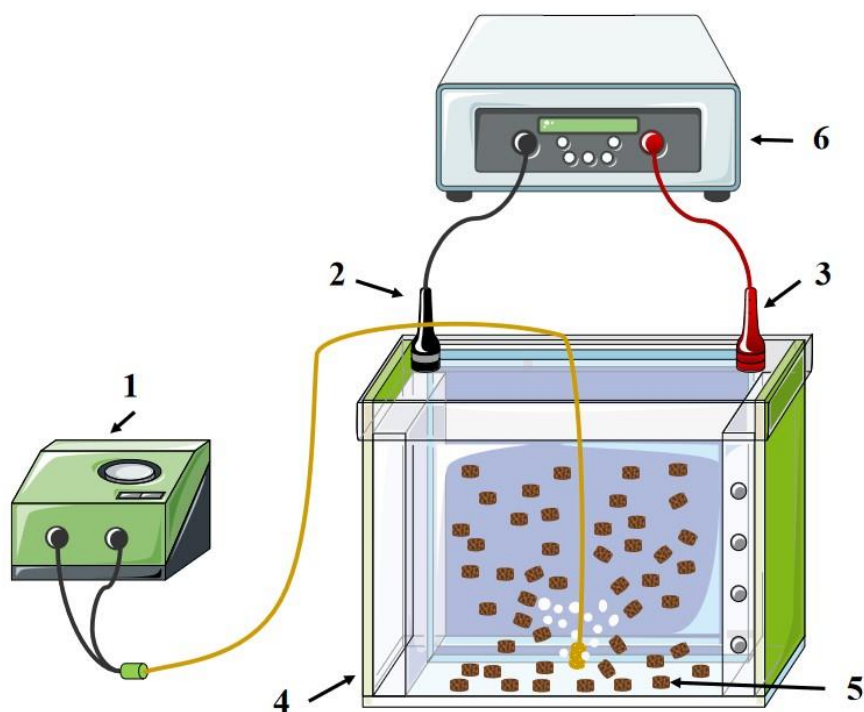
Figure S1. Schematic of the three-dimensional electrochemical system. (1) aeration system, (2) cathode plate, (3) anode plate, (4) electrolytic cell, (5) particle electrodes, (6) power supply.

EDX characterization


Figure S2. The EDS images of 3D-CPE

The EDS elemental spectrum of 3D-CPE indicated the presence of Fe, Co, Ni, P, C and N (Fig. S2), which suggested that the Fe-Co-Ni-P was successfully supported on the pristine g-C_3N_4.

Py-IR spectra of Fe-Co-Ni-P/g-C_3N_4 particles

Table S1 Distribution of L and B acid sites determined by Py-IR.

Temperature (°C)	Amount of B acid (μmol/g)	Amount of L acid (μmol/g)	Total acid (μmol/g)	B/L
100	1.13	41.38	42.51	0.03
200	0.66	17.76	18.42	0.04
300	0.38	6.66	7.04	0.06

Investigation on the material stability
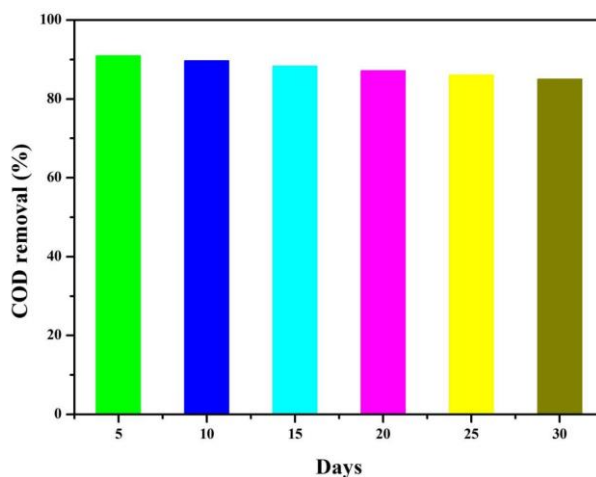
Figure S3. COD removal efficiency in continuous runs of 3D-CPE system.

BET characterization

The BET surface area of Fe-Co-Ni-P/g-C$_3$N$_4$ particles was 45.66 m^2/g, which was lower than that of pristine g-C$_3$N$_4$ with 92.56 m^2/g. It can be expected that these abundant pores originated from g-C$_3$N$_4$ may provide more exposed active sites for 3D-CPE system. The pure Fe-Co-Ni-P particles was well dispersed onto the g-C$_3$N$_4$ porous layer, so the BET surface area of pristine g-C$_3$N$_4$ was decreased.

Four-probe resistivity test

The resistivity of the Fe-Co-Ni-P/g-C$_3$N$_4$ particles was measured with a four-probe resistivity meter. Compared with the low impedance conductive particles, the as-prepared Fe-Co-Ni-P/g-C$_3$N$_4$ particles show more resistivity (1.2×10^5 Ω·cm). High impedance electrode particles were charged via electrostatic induction of the electric field. The charged particles on the surface become independent 3D electrodes, and the corresponding electrochemical oxidation and reduction reactions take place at two ends of the particles, respectively. Each charged particle forms a "micro electrolysis cell", thus considerably enhancing the area of the electrochemical reaction. Meanwhile, high impedance conductive particles avoid the short-circuit current, accelerate the mass transfer, and promote the electrocatalytic degradation [42].

Energy consumption

The Energy consumption (EC) is generally utilized to express the electrochemical oxidation performance of quinoline, which can be calculated by Eq. (1).

$$EC = \frac{1000UIt}{(C_0 - C_t) \times V}$$

where EC is energy consumption (kWh/kg quinoline), U is the cell voltage (V), I is the current (A), t is the electrolysis time (h), V is the volume of wastewater (L), and C$_0$ (mg/L) and C$_t$ (mg/L) are the quinoline concentrations at treatment time 0 and t, respectively [54].

In this study, it was measured that the initial concentration of quinoline was 3000 mg/L. Under the optimal conditions, the concentration of quinoline degraded by 2D-EF system for 30 minutes was 1008.6 mg/L, and that of quinoline degraded by 3D-CPE process for 30 minutes was 271.5 mg/L. Under the optimal conditions, voltage 25 V, current 5 A, time 30 min, volume 2 L was substituted into the above formula. The energy consumption of 3D-CPE process was 11.45 kWh/kg quinoline, which is significantly lower than that of 2D-EF system (15.69 kWh/kg quinoline). On the one hand, the addition of the particle electrode increased the oxidation activity and produced a large number of hydroxyl radicals to improve the degradation efficiency of quinoline. on the other hand, it is obvious that the treatment of wastewater with high pollutant concentration can achieve low energy consumption [18].

HPLC-MS analysis

Figure S4 showed the total ion current chromatograph of quinoline and degradation intermediates by HPLC-MS under the optimal process conditions in positive ion mode. Seven peaks were observed at 1.732, 3.042, 4.103, 5.031, 6.988, 7.966 and 11.581 min, respectively. Except the peak formed by quinoline at 3.042 min, other peaks were assumed to be related to oxidation intermediates of quinoline degradation. Figure S5 showed the mass spectra in different retention times in positive ion mode. The peaks at m/z=146, 130, 134 and 150 were related to the protonated intermediates and quinoline, respectively. The possible molecular structure of the degradation products were deduced, as shown in Table 1.
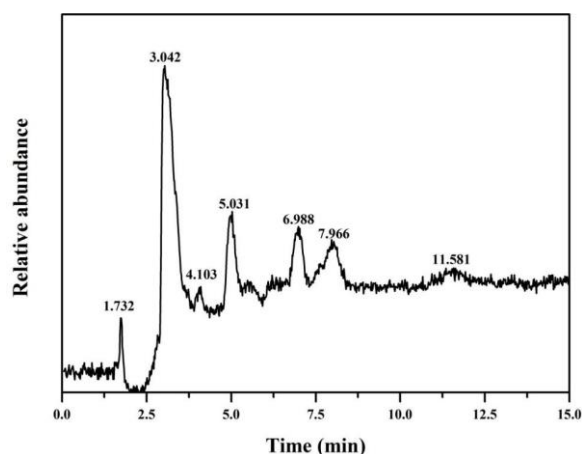

Figure S4. Total ion current chromatograph of quinoline and degradation products by HPLC-MS in positive ion mode.
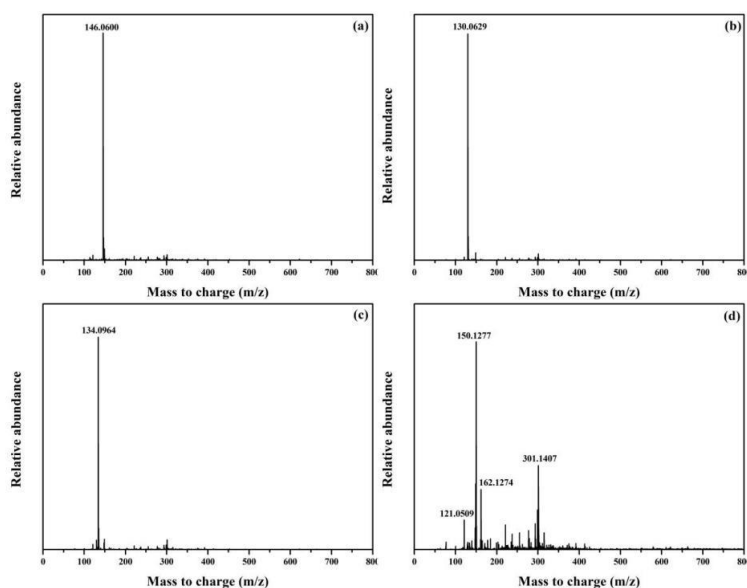
Figure S5. Mass spectra of quinoline degradation in different retention times: (a) 1.682~1.798 min; (b) 2.926~3.622 min; (c) 4.816~5.297 min; (d) 11.266~12.012 min in positive ion mode.

Sum of electronic and thermal Free Energies

The thermodynamic function, Gibbs free energy was used to determine the reaction direction. Figure S6 showed the chemical reaction equation of quinoline under the action of hydroxyl radical, and the Gibbs free energy of part of the equation was derived according to the theory of computational chemistry.
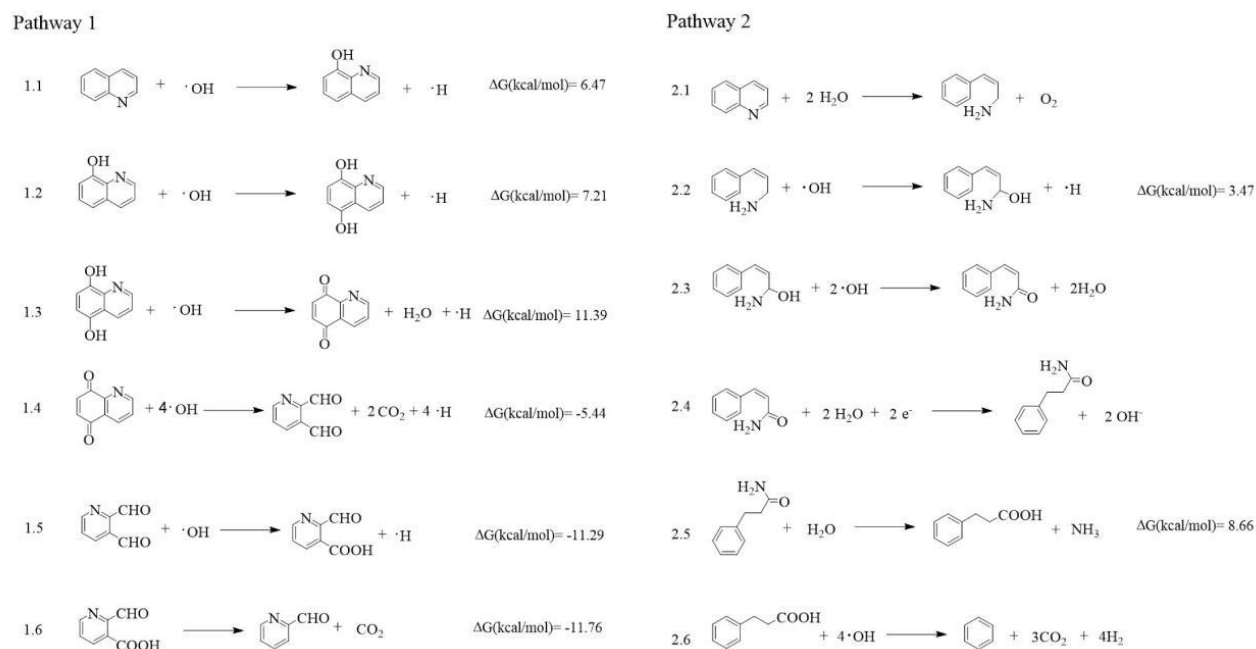
Figure S6. Reaction equation and partial Gibbs free energy.

DECLARATION OF COMPETING INTEREST
The authors declare that they have no known competing financial interests or personal relationships that could have appeared to influence the work reported in this paper.

References

1. D. Rameshraja, V. C. Srivastava, J. P. Kushwaha and I. D. Mall, *Chemical Engineering Journal*. 181 (2012) 343-351.
2. Y. Luo, X. Yue, P. Wei, A. Zhou and S. Alimzhanova, *Science of The Total Environment*. 747 (2020) 9 141136.
3. M. Olak-Kucharczyk, M. Foszpańczyk, R. Żyłła and S. Ledakowicz, *chemosphere*. 291 (2021) 132742.
4. K. Zhi, C. Yang, Y. Zheng, R. Zhang, O. T. E, H. Wu and Z. Jiang, *Ind. Eng. Chem. Res.*, 61 (2022)

23 8141-8148.

5. A. Santos, P. Yustos, A. Quintanilla, F. García-Ochoa and J. Rodríguez, *Environmental Science and Technology*. 38 (2004) 1 133-138.
6. Y. Xu, Y. S. Qian, J. L. Qiao, D. Y. Huang and S. B. Cui, *Int. J. Electrochem. Sci.*, 17 (2022) 22024.
7. M. Klavarioti, D. Mantzavinos and D. Kassinos, *Environment International*. 35 (2009) 2 402-417.
8. P. Fernández-Castro, M. Vallejo, M. F. San Román and I. Ortiz, *Journal of Chemical Technology & Biotechnology*. 90 (2015) 5.
9. B. Tutunaru and B. Oprea, *Int. J. Electrochem. Sci.*, 17 (2022) 1.
10. E. Alfaya, O. Iglesias, M. Pazos and M. A. Sanromán, *RSC Advances*. 5 (2015) 19 14416-14424.
11. G. Zhang, S. Wang and F. Yang, *Journal of Physical Chemistry C*. 116 (2012) 5 3623–3634.
12. W. Zhang, D. Xie, X. Li, W. Ye, X. Jiang, Y. Wang and W. Liang, *Applied Catalysis A: General*. 559 (2018) 75-84.
13. W. Liu, Z. Ai and L. Zhang, *Journal of Hazardous Materials*. 243 (2012) DEC. 257-264.
14. B. Hou, B. Ren, R. Deng, G. Zhu, Z. Wang and Z. Li, *RSC Advances*. 7 (2017) 15455-15462.
15. W. Kong, B. Wang, H. Ma and L. Gu, *Journal of Hazardous Materials*. 137 (2006) 3 1532-1537.
16. M. Li, F. Zhao, M. Sillanpää, Y. Meng and D. Yin, *Separation & Purification Technology*. 156 (2015) 588-595.
17. L. f. Hong, R. t. Guo, Y. Yuan, X. y. Ji, Z. d. Lin, Z. s. Li and W. g. Pan, *ChemSusChem*. 14 (2020) 2 539-557.
18. Y. Liu, Y. Ma, J. Wan, Y. Wang and Y. Xue, *Environmental Science and Pollution Research*. 28 (2021) 43815-43830.
19. Arne, Thomas, Anna, Fischer, Frederic, Goettmann, Markus, Antonietti, Jens-Oliver and Müller, *Journal of Materials Chemistry*. 18 (2008) 41 4893-4908.
20. W. Sufang, Z. Aijuan, Z. Jiaguang, Z. Zheng and J. Zhao, *RSC Advances*. 9 (2019) 1176-1186.
21. X. Wang, K. Maeda, A. Thomas, K. Takanabe and M. Antonietti, *Nature Materials*. 8 (2009) 76-80.
22. Chaiti, S. Chan, Bingjun, Kundu, Aniruddha, Park, J. Hyeok and S. Chan, *ACS Sustainable Chemistry & Engineering*. 6 (2018) 5 6146-6156.
23. Z. W. Zhao, T. Wen, K. Liang, Y. F. Jiang, X. Zhou, C. C. Shen and A. W. Xu, *Acs Appl Mater Interfaces*. 9 (2017) 4 3757-3765.
24. J. Liu, S. Wang, J. Xuan, B. Shan, H. Luo, L. Deng, P. Yang and C. Qi., *Tungsten*. 4 (2022) 38-51.
25. Z. Tahmasebi, A. M. Zardkhoshoui and S. Davarani, *Catalysis Science & Technology*. 11 (2021) 1814-1826.
26. Q. Liu, S. Gu and C. M. Li, *Journal of Power Sources*. 299 (2015) 342-346.
27. Z. Sun, H. Zheng, P. Du and J. Li, *Energy & environmental science*. 8 (2015) 2668-2676.
28. J. Xiao, Q. Y. Lv, Y. Zhang, Z. Zhang and S. Wang, *Rsc Advances*. 6 (2016) 107859-107864.
29. L. Songsong, W. Lu, L. Shuang, X. Boran, X. Nan, G. Yangqin, S. Weiyu, G. Lei and L. Jian, *ACS Sustainable Chemistry & Engineering*. 6 (2018) 8 9940-9950.
30. J. Yang, D. Guo, S. Zhao, Y. Lin, R. Yang, D. Xu, N. Shi, X. Zhang, L. Lu and Y. Q. Lan, *Small*. 15 (2019) 10.
31. Z. Sun, M. Zhu, X. Lv, Y. Liu, C. Shi, Y. Dai, A. Wang and T. Majima, *Applied Catalysis B: Environmental*. 246 (2019) 330-336.
32. J. Chen, P. Gang, Z. Wei, Z. Wenbo, G. Li and W. Xiaoqin, *Catalysis Science & Technology*. 10 (2020) 7399-7399.
33. Y. P. Wang, Y. H. Liu, R. Ruan, S. T. Liu, P. W. Wen and Y. Q. Wan, *Synthesis and Reactivity in Inorganic and Metal-Organic Chemistry*. 46 (2016) 10 1506-1512.
34. Agarwal, Bhumica, Kailasam, Kamalakannan, Sangwan, Rajender, Singh, Elumalai and Sasikumar, *Renewable and Sustainable Energy Reviews*. 82 (2018) 2408-2425.
35. W. Zhang, J. Chen, J. Wang, C. Cui, B. Wang and Y. Zhang, *Water*. 13 (2021) 128.
36. Z. A. Chao, L. A. Feng, B. Hz, A. Rw, B. Xy, A. Yy, A. Jh, B. Ggy and B. Mh, *Journal of*

Int. J. Electrochem. Sci., 17 **(2022)** Article Number: 221296

21

Hazardous Materials. 420 (2021) 126556.

37. M. Li, X. Qin, J. Cui, R. Guo, C. Guo, Z. Wang and T. Li, *Journal of Environmental Chemical Engineering*. 9 (2021) 4 105573.
38. A. Jorge, Delgado, S. Castillón, D. Curulla-Ferré, C. Claver and C. Godard, *Catalysis Communications*. 71 (2015) 5 88-92.
39. F. Moreira, A. Rui, E. Brillas and V. Vilar, *Applied Catalysis B: Environmental*. 202 (2017) 217-261.
40. V. Oskoei, M. H. Dehghani, S. Nazmara, B. Heibati and V. K. Gupta, *Journal of Molecular Liquids*. 213 (2016) 374-380.
41. S. Liu, Z. Wang, J. Li, C. Zhao and X. He, *Chemosphere*. 213 (2018) 377-383.
42. Hong Li, Hai Yang, Jia Cheng, Hu Chao and Yang Ze, *Journal of Cleaner Production* 308 (2021) 127324.
43. F. Mogyoródy, *Journal of Applied Electrochemistry*. 36 (2006) 6 635-642.
44. C. Guo, H. Liu, C. Wang, J. Zhao and Y. N. Zhang, *Environmental Pollution*. 260 (2020) 114101.
45. Y. Wang, Z. Shen and X. Chen, *Journal of Hazardous Materials*. 178 (2010) 1-3 867-874.
46. N. G. Yasri, A. Yaghmour and S. Gunasekaran, *Journal of Environmental Chemical Engineering*. 3 (2015) 2 930-937.
47. M. Tong, S. Yuan, S. Ma, M. Jin, D. Liu, D. Cheng, X. Liu, Y. Gan and Y. Wang, *Environmental Science & Technology*. 50 (2015) 9 4890-4891.
48. Y. Xie, X. Wang, W. Tong, W. Hu, P. Li, L. Dai, Y. Wang and Y. Zhang, *Chemical Engineering Journal*. 396 (2020) 125321.
49. J. Peller, O. Wiest and P. V. Kamat, *The Journal of Physical Chemistry A*. 105 (2001) 13.
50. B. Zhang, Y. Hou, Z. Yu, Y. Liu, J. Huang, L. Qian and J. Xiong, *Separation and Purification Technology*. 210 (2018) 60-68.
51. C. Ma, S. Feng, J. Zhou, R. Chen and S. Wang, *Applied Catalysis B: Environmental*. 259 (2019) 118015.
52. Jun Chen, Boding Zhang, Bingxing Wang, Wenlong Zhang, Jichao Wang, Chengxing Cui and Songlin Wang, *Environmental Science and Pollution Research*. 22 (2022) 22232-22234.
53. J. Zhao, Z. Xian, G. Hai, H. Dong, Y. Hong, L. Yunqi and G. Xu, *Journal of Industrial and Engineering Chemistry*. 105 (2021) 49-57
54. Y. Sun, P. Li, H. Zheng, C. Zhao, X. Xiao, Y. Xu, W. Sun, H. Wu and M. Ren, Chemical Engineering Journal. 308 (2017) 1233-1242.